NUMERICAL SIMULATION OF UNDEREXPANDED SONIC JET

Malsur Dharavath and Debasis Chakraborty
Directorate of Computational Dynamics
Defence Research and Development Laboratory
Kanchanbagh Post
Hyderabad - 500 058, India
Email : debasis_cfd@drdl.drdo.in

Abstract

Underexpanded sonic jet is numerically simulated using commercial CFD software. Three dimensional Navier Stokes equations alongwith two equation turbulence models are solved. Computed centerline distribution and profiles of various flow variables at various axial stations agree quantitatively with experimental results. The comparison of the flow variables computed with four different two equation models reveals that k - ε and RNG k - ε models perform very well in predicting both pressure and temperature throughout the flow filed; whereas SST and k - ω models fail to predict the flow behavior beyond the first Mach disc.

Introduction

Sonic and supersonic jets are of interest from the point of view of fundamental fluid mechanics as well as practical applications. Underexpanded sonic jets are often used in high-performance nozzles of missiles and rockets, scramjet combustor, chemical lasers etc. A thorough knowledge of the global structure and the dynamics of these flows are important in the future development of air and space propulsion systems. Better understanding of the jet structure can lead to reduced thermal signature and jet noise. The underexpanded sonic jet is treated as a canonical problem in the literature and efforts are continuing to have better understanding of its structure.

The schematic of the underexpanded sonic jet flow field is shown in Fig.1. The underexpanded jet flowfield contains viscous and inviscid regions, normal and oblique shocks, and regions of expansion and compression waves. As the static pressure at jet exit is greater than the ambient pressure, flow at the exit of the jet is accelerated by the Prandtl-Meyer expansion fan centered at the lip of the jet nozzle. In the downstream, the atmospheric constant pressure boundary redirects the expansion waves towards the jet centerline as a series of compression waves which in turn coalesce to form the oblique intercepting shock. This barrel-like shock, separating the inner jet core from the outer sheath of supersonic fluid, terminates at the Mach disk. The outer jet region persists downstream of the Mach disk and the near-field shock system repeats itself downstream, forming a number of weaker shock cells. The compressible shear layer at the outer edge of the jet grows with downstream distance and the jet eventually transit to a fully-developed turbulent stream in the far field.

The underexpanded jet flowfield has been studied theoretically, experimentally and computationally since last few decades. Englert [1] used series solution to provide an operational method for determining the initial contour and pressure field about a supersonic jet. Previous numerical studies often relied on the method of characteristics (MOC) [2-4] for determining the inviscid jet velocity field, centreline Mach number distribution and Mach disk location as a function of stagnation pressure over a range of flow conditions in both sonic and supersonic underexpanded jets. Measurements in sonic/supersonic jets are difficult because of nonsuitability of direct measurement method, due to varying static pressure, high velocities and shocks. Nonintrusive flow measurement techniques, namely Laser Doppler Anemometry and Laser Induced Fluorescence have been employed to measure various flow parameters in the underexpanded jet [5-9]. Woodmansee, Dutton and Lucht [10] used high-resolution N_2 CARS technique to obtain mean pressure, temperature, and density measurements in the flowfield of an underexpanded jet. Time averaged CARS measurements have been acquired along the centerline and for radial traverses at a number of streamwise locations in the underexpanded

Paper Code : V64 N4/771-2012. Manuscript received on 23 Jan 2012. Reviewed and accepted as a Full Length Contributed Paper on 03 Sep 2012

jet flowfield. Reliable measurement of velocity and turbulent quantities of the underexpanded jet is still very limited for the validation of computational model.

With the advent of powerful computer and advanced numerical techniques, CFD methods have become matured and are increasingly being used in aerospace designs and in complex flow physics exploration. Various Euler [11] and Parabolised Navier Stokes (PNS) [12, 13] methods are employed in the simulation of underexpanded jet and these methods overpredict the shock structure and underpredict the mixing rate. NavierStokes calculations [14] with k-ε turbulence model showed promising results to capture the underexpanded jet flow structure. Birkby and Page [15] used Navier Stokes equations and k-ε turbulence model with compressibility corrections to simulate underexpanded jet flow field using a pressure based methodology. Their simulations predict correct shock - cell wavelength but decay was too rapid compared to the experimental results. The comparison of Fluorescence Imaging of underexpanded jet by Wilkes et al. [16] with CFD results from GASP (General Aerodynamic Simulation Program) [17] revealed that although for lower jet pressure ratios, the jet primary wave length agrees with the experimental results but for higher pressure ratio, the computed Mach disk diameter and Mach disk location differ from the experimental results by 35% and 15 % respectively. It is clear that underexpanded jets need to be analyzed in greater detail and the role of various turbulence models need to be studied for accurate prediction of the jet characteristics.

In this work, experimental condition of Woodmansee et al. [10] is simulated numerically and the centerline distribution and radial profiles at different cross sections of various flow parameters are compared with experimental values. The capabilities of different two equation turbulence models were also assessed in predicting the radial profiles of underexpanded sonic jet.

Experimental Condition for Which the Simulation is Carried Out

The present simulation explore the experimental condition of Woodmansee et al. [10] where the center line and radial profiles of mean pressure, temperature, and density of an underexpanded jet is measured using a high-resolution N_2 CARS technique. The underexpanded jet flowfield is generated using a converging nozzle attached to a high-pressure flow system. Upstream of the converging nozzle, the stagnation temperature and pressure are measured. The jet facility is moved with respect to the stationary probe volume, instead of translating the CARS probe volume to different positions in the jet flowfield. The jet operating conditions are summarized in Table-1. The jet with a Reynolds number of 1.31×10^5 is operated with a nozzle pressure ratio (P_t / p_∞) of 6.17. The relatively large convective Mach number (Mc = 0.8), shows that the shear layer experienced substantial compressibility effect. Upstream of the Mach disk, the CARS centerline measurement locations are spaced by 356 μm, whereas the spacing between the measurement locations is doubled in the downstream of the Mach disc. The radial profiles are measured at locations corresponding to x/d_j of 0.0, 1.28, 1.56, 3.0, and 4.0 as shown in Fig.2. The profile locations are chosen so that jet structure near nozzle exit, mach disk and the farfield region could be clearly distinguished.

Computational Methodology

CFX-10 [18] is an integrated software system capable of solving diverse and complex multidimensional fluid flow problems. The software solves three dimensional Reynolds Averaged Navier Stokes (RANS) equations in a fully implicit manner. It is a finite volume method and is based on a finite element approach to represent the geometry. The method retains much of the geometric flexibility of finite element methods as well as the important conservation properties of the finite volume method. The software has four major modules a) *CFX Build*, imports CAD geometry or creates geometry and generates unstructured volume meshing based on the user input b) *preprocessor* - sets up the boundary condition and initial field condition c) *solver manager* - solves the flow field based on the grid and the boundary condition and d) *postprocessor* - visualizes and extracts the results. It utilizes numerical upwind schemes to ensure global convergence of mass, momentum, energy and species. In the present study, the discreti-

Table-1 : Inflow Parameters for Underexpanded Jet

Parameters	Values
Jet stagnation pressure (P_t) [atm]	6.05
Jet stagnation temperature [K]	296
Jet Reynolds Number (Re_j) [million]	0.13
Convective Mach Number (M_c)	0.8
Nozzle exit diameter (d) [mm]	5.0
Nozzle convergent angle (deg)	20
Free stream pressure (p_∞) [atm]	0.98
Free stream temperature [K]	294

sation of the convective terms is done by second order upwind difference scheme. Local time stepping has been used to obtain steady state solutions. Baseline calculations are done with k-ε turbulence model [19] with wall function. Three different two-equation turbulence turbulence models namely k-ω [20] and SST [21], RNG based k-ε turbulence model [22] are also simulated for assessing the predictive capabilities of these models in predicting underexpanded jet structures. In RNG k-ε model, the dissipation rate transport equation models the rate of strain rate that may be important for the treatment of nonequilibrium flows and flows in rapid distortion limit such as massively separating flow and stagnation flow. To find out the accuracy and the range of applications, the software has been validated extensively for various complex flows including supersonic base flows [23], transverse injection in supersonic flow for missile control [24] etc and very good quantitative agreement with the experimental results are obtained The details of governing equations, turbulence models and the discretisation schemes are given in the following subsections.

Governing Equations

The appropriate system of equations governed the turbulent compressible gas may be written as

Continuity equation :

$$\frac{\partial \rho}{\partial t} + \frac{\partial}{\partial x_k}(\rho u_k) = 0 \quad k = 1, 2, 3$$

Momentum equation :

$$\frac{\partial}{\partial t}(\rho u_i) + \frac{\partial}{\partial x_k}(\rho u_i u_k) + \frac{\partial p}{\partial x_i} = \frac{\partial(\tau_{ik})}{\partial x_i}, \quad i, k = 1, 2, 3$$

Energy equation :

$$\frac{\partial}{\partial t}(\rho E) + \frac{\partial}{\partial x_k}(\rho u_k H) = -\frac{\partial}{\partial x_k}(u_j \tau_{jk}) + \frac{\partial q_k}{\partial x_k}, \quad j, k = 1, 2, 3$$

where, ρ , u_i , p , E and H are the density, velocity components, pressure and total energy and total enthalpy respectively Turbulent shear stress is defined as

$$\tau_{ik} = \mu\left(\frac{\partial u_i}{\partial x_k} + \frac{\partial u_k}{\partial x_i}\right)$$

$\mu = \mu_l + \mu_t$ is the total viscosity ; μ_l , μ_t being the laminar and turbulent viscosity

Laminar viscosity (μ_l) is calculated from Sutherland law as

$$\mu_l = \mu_{ref}\left(\frac{T}{T_{ref}}\right)^{3/2}\left(\frac{T_{ref}+S}{T+S}\right)$$

where, T is the temperature and μ_{ref} , T_{ref} and S are known coefficient.

In eddy viscosity models, the stress tensor is expressed as a function of turbulent viscosity (μ_t). Based on dimensional analysis, few variables (k, ε, ω) are defined as given below,

Turbulent kinetic energy k,

$$k = \overline{u'_i u'_i}/2$$

Turbulent dissipation rate ε,

$$\varepsilon \equiv \overline{\nu \frac{\partial u'_i}{\partial x_j}\left(\frac{\partial u'_i}{\partial x_j} + \frac{\partial u'_j}{\partial x_i}\right)}$$

Specific dissipation rate ω,

$$\omega = \frac{\varepsilon}{k}$$

The turbulent viscosity μ_t is calculated as

$$\mu_t = c_\mu \frac{\rho k^2}{\varepsilon}$$

The heat flux q_k is calculated as $q_k = -\lambda \frac{\partial T}{\partial x_k}$, λ is the thermal conductivity

k-ω Turbulence Model

The turbulent viscosity is calculated as function of k and ω [20].

$$\mu_t = f\left(\frac{\rho k}{\omega}\right)$$

Turbulent kinetic energy (k) equation :

$$\frac{\partial}{\partial t}(\rho k) + \frac{\partial}{\partial x_i}(\rho k u_i) = \frac{\partial}{\partial x_j}\left(\Gamma_k \frac{\partial k}{\partial x_j}\right) + G_k - Y_k$$

Specific dissipation rate (ω) equation :

$$\frac{\partial}{\partial t}(\rho \omega) + \frac{\partial}{\partial x_i}(\rho \omega u_i) = \frac{\partial}{\partial x_j}\left(\Gamma_\omega \frac{\partial \omega}{\partial x_j}\right) + G_\omega - Y_\omega$$

Where G_k, Y_k, Γ_k and G_ω, Y_ω, Γ_ω are the production, dissipation and diffusion terms of the k and ω equations respectively.

SST Turbulence Model

To retain the robust and accurate formulation of Wilcox's k-ω model in the near wall region, and to take advantage of the freestream independence of the k-ε model in the outerpart of the boundary layer, Menter [21] blended both the models through a switching function. k-ε model was transformed into Wilcox's k-ω formulation and was multiplied by (1-F_1) and added to original k-ω model multiplied by F_1 . The blending function F_1 will be one in the near wall region and zero away from the surface. .In the second step, the definition of eddy viscosity was modified in the following way to account for the

$$v_t = \frac{a_1 k}{\max(a_1 \omega ; \Omega F_2)}$$

transport of the principal turbulent shear stress ($\tau = \overline{-\rho u' v'}$)

Renormalized Group (RNG) k-ε Model

An improved method for rapidly strained flows based on rigorous statistical technique [22] is also used in the present calculations. The k and ò equations are given below :

$$\frac{\partial}{\partial t}(\rho k) + \frac{\partial}{\partial x_i}(\rho k u_i) = \frac{\partial}{\partial x_j}\left(\alpha_k \mu_{eff} \frac{\partial k}{\partial x_j}\right) + G_k - \rho \grave{o} - Y_M$$

$$\frac{\partial}{\partial t}(\rho \grave{o}) + \frac{\partial}{\partial x_i}(\rho \grave{o} u_i) = \frac{\partial}{\partial x_j}\left(\alpha_{\grave{o}} \mu_{eff} \frac{\partial \grave{o}}{\partial x_j}\right) + C_{1\grave{o}} \times \frac{\grave{o}}{k} \times G_k - C_{2\grave{o}} \rho \frac{\grave{o}^2}{k} - R_{\grave{o}}$$

Where G_k is the generation of turbulence kinetic energy due to the mean velocity gradients, calculated as $G_k = -\rho \overline{u'_i u'_j} \frac{\partial u_j}{\partial x_i}$ and Y_M represents compressibility effects given by, $Y_M = 2 \rho \grave{o} M_t^2$. The turbulent Mach number M_t is given by $M_t = \sqrt{k/a^2}$.

The model constants are taken as,
$C_{1\grave{o}} = 1.42$, $C_{2\grave{o}} = 1.68$, $C_\mu = 0.0845$, $\sigma_k = \sigma_{\grave{o}} = 1.393$

The additional term in ε equation R_ε is given as

$$R_{\grave{o}} = \frac{C_\mu \rho \eta^3 (1 - \eta/\eta_o)}{1 + \beta \eta^3} \frac{\grave{o}^2}{k},$$

where $\eta \equiv Sk / \grave{o}$, $\eta_o = 4.38$ and $\beta = 0.012$.

Discretisation of Governing Equations

The CFX-TASCflow solver utilizes a finite volume approach, in which the conservation equations in differential form are integrated over a control volume described around a node, to obtain an integral equation. The pressure integral terms in momentum integral equation and the spatial derivative terms in the integral equations are evaluated using finite element approach. An element is described with eight neighboring nodes. The advective term is evaluated using upwind differencing with physical advection correction. The set of discretised equations form a set of algebraic equations: $A \vec{x} = b$ where $\vec{x}$ is the solution vector. The solver uses an iterative procedure to update an approximated x_n (solution of x at n^{th} time level) by solving for an approximate correction x' from the equation $A \vec{x'} = \vec{R}$, where $\vec{R} = \vec{b} - A \vec{x_n}$ is the residual at n^{th} time level. The equation $A \vec{x'} = \vec{R}$ is solved approximately using an approach called Incomplete Lower Upper factorization method.

Results and Discussions

Taking the advantage of the symmetry of the flowfield, only one quadrant of the flowfield is simulated. The nozzle geometry and the computational domain are shown in Fig.3. The X, Y and Z axes are taken along the longitudinal, height and lateral directions respectively and the origin is taken at the centerline of the nozzle at the exit plane. The computational domain is extended to 103 times the nozzle diameter (103d) in the longitudinal direction and 20d in the both lateral and height direction. The free stream

inflow plane is placed at 4d upstream of the nozzle exit plane. A Very fine structured grid of 3.7 million size (292 x 90 x 85) is generated in the flowfield. To capture the initial growth of the jet very fine mesh are employed near the inflow and the centerline. The grids are made progressively coarser as we proceed downstream and the far field boundary. The typical computational grid is shown in Fig.4. Grid independence of the results are studied by carrying out the simulation with another grid of 1.84 million size (240 x 90 x 85) and comparing the results. (Grid independence of the results are discussed later). Stagnation pressure (6.05 atm) and stagnation temperature (296K) are specified in the convergent section of the nozzle and free stream pressure (0.98 atm) and temperature (294 K) are specified in the free stream inflow plane. Pressure and supersonic boundary conditions are prescribed for the farfield and outflow boundaries respectively. A log normalized residue of 10^{-6} is considered as the convergence criteria for mass, momentum and energy equations.

The qualitative features of the flow field are depicted through the Mach number and temperature distributions in the symmetry plane of the flow field in Fig.5. All the essential features of the flow field including Mach discs, barrel shocks, shock cells are crisply captured in the simulation. Computed centerline distribution of pressure, temperature and pressure profile at x/D =4.0 are compared for two different grids and experimental values in Fig.6. It can be observed that by changing the grid from 1.84 million to 3.67 million the results do not vary significantly thus demonstrating the grid independence of the results.

Simulations are carried out with four different two equation turbulence models namely, (1) k-ε (2) k-ω (3) SST and (4) RNG k-ε to assess their capabilities in simulating underexpanded jet. The axial distributions of centerline pressure and temperatures with different turbulence models are compared with experimental results Figs.7a and 7b respectively. A very good comparison is obtained between the experimental and numerical values obtained with k-ε and RNG k-ε models . The computed locations of the first two Mach discs match extremely well with the experimental data. Downstream of the second recompression region (x/D > 3.5) the computed pressure data show a plateau, while the experimental data is showing wavy trend. The maximum difference of computed and experimental pressure values are of the order of 10% (same as the experimental uncertainty as reported in Ref.10). All turbulence models captured the overall trend of the experimental results. The k-ε and RNG k-ε models followed the similar pattern throughout the computational length and match the experimental pressure extremely well. The SST and k-ω models show higher pressure beyond x/d > 2.0. SST model could not predict centerline temperature beyond x/D > 3.

The pressure profiles at x/d = 0, 1.28, 1.56, 3.0 and 4.0 are compared between experimental and different turbulence model in Fig.8. It is observed in the figures that upto the first shock cell (Upto x/d =1.28), all the turbulence models showing the similar trend. But downstream of the first Mach disc, SST and k-ω models fail to capture the experimental trends. Both k-ε and RNG k-ε models predict the experimental pressure profiles reasonably well upto x/d = 3.0. In the last axial station (x/d = 4.0), none of the turbulence models in able to predict centerline variation of the pressure. At the nozzle exit (Fig.8a, although trend of the pressure profile is captured, computed pressure under predict the experimental value by about 12%. In the middle of the first shock cell, the jet structure is well behaved and the computations agree very well with the experimental value. In the recompression region of 1st Mach disc (Fig.8c), the computation captures the experimental trend reasonably well, although the crest and valley of the experimental pressure is higher than the computational result in the zone (0 < y/d < 0.4). At X/d =3.0, (Fig.8d) the comparison is very good except the dip in experimental pressure at y/D = 0.7. The computation could not capture the pressure profile at the second Mach disc location at x/D =4.0 (Fig.8e). Although the jet width is captured, computed pressure profile is showing a plateau region compared to intense shock interactions in the centerline region. The cause of this mismatch could not be explained. The experimental temperature profiles at the same axial stations are compared with different turbulence model in Fig.9. Temperature profiles are seen to match the experimental values quite nicely. Maximum deviations between the computed and the experimental values with k-ε turbulence model are of the order 10 K. Turbulence models exhibit similar trends for temperature prediction also. Both k-ε and RNG k-ε models predict the experimental temperature profiles for all the axial stations; while the performance of SST and k-ω models are not statisfactory for the prediction the temperature profiles for axial stations downstream of the first Mach disc.

Conclusions

Numerical explorations are carried out for underexpanded sonic jet using commercial CFD solvers. Three

dimensional Navier Stokes equations are solved alonwith two equation turbulence model. Simulation captures all the essential flow features including Mach discs, barrel shocks etc. Very good match has been obtained with experimental data for centerline distribution of all the variables. Computed temperature profiles match very nicely with the experimental values at different axial stations. Although, pressure profiles at near field axial locations match nicely with the experimental values, some deviations are observed for the core pressure in the farfield axial stations. Four different turbulence models were studied to assess their predictive capabilities for underexpanded sonic jet and all the turbulence models predicts the profiles and centerline values of pressure and temperature upto the first Mach disc very well. Both k-ε and RNG k-ε models predict the experimental temperature profiles for all the axial stations very well, but the performance of SST and k-ω models are not very good in predicting temperature and pressure profiles in the far field region beyond first Mach disc.

References

1. Englert, G.W., "Operational Method of Determining Initial Contour of and Pressure Field about a Supersonic Jet", NASA TND 279, 1960.

2. Adamson, T.C., Jr, and Nicholls, J.A., "On the Structure of Jets from Highly Underexpanded Nozzles into Still Air", Journal of Aerospace Sciences, Vol 26, No.1, 1959, pp.16-24.

3. Fox, J.H., "On the Structure of Jet Plumes", AIAA Journal Vol.12, No.1, January 1974, pp.105-107.

4. Abbett, M., "The Mach Disk in Underexpanded Exhaust Plumes", AIAA Journal, Vol.9, No.3, March 1971, pp.512-514.

5. Adrian, R. J., "Laser Velocimetry", in Fluid Mechanics Measurements, R.J. Goldstein, ed., Taylor and Francis, 1996, pp.175-293.

6. Eggins, P.L. and Jackson, D.A., "Laser- Doppler Velocity Measurementsin an Under-Expanded Free Jet", Journal of Physics D: Applied Physics, Vol.7, 1974, pp.1894-1906.

7. Krothapalli, A., Buzyna, G. and Lourenco, L., "Streamwise Vortices in an Underexpanded Axisymmetric Jet", Physics of Fluids A, Vol.3, No.8, 1991, pp.1848-1851.

8. Chuech, S.G., Lai, M.C. and Faeth, G.M., "Structure of Turbulent Underexpanded Free Jets", AIAA Journal, Vol.27, 1989, pp.549-559.

9. Wilkes, J.A., Glass, C.E., Danehy, P.M. and Nowak, R. J., "Fluorescence Imaging of Underexpanded Jets and Comparison with CFD", AIAA Paper No. 2006-910, 2006.

10. Woodmansee, M. A., Dutton, J.C. and Lucht, R.P., "Experimental Measurements of Pressure, Temperature, and Density in an Underexpanded Sonic Jet Flowfield, AIAA Paper No.99-3600, 1999.

11. Matsuda, T., Umedy, Y., Ishii, R., Yasuda, A. and Sawada, K., "Numerical and Experimental Studies on Choked Underexpanded Jets" AIAA Paper No.87-1378, 1987.

12. Dash, S. M., Wolf, D.E. and Seiner, J.M., "Analysis of Turbulent Underexpanded Jets, Part-1: Parabolized Navier - Stokes Model, SCIPVS", AIAA Journal, Vol.23, No.4, April 1985, pp.505-514.

13. Abdol-Hamid, K.S. and Wilmoth, R.G., "Multiscale Turbulence Effects in Underexpanded Supersonic Jet", AIAA Journal, Vol.27, 1989, pp.315-322.

14. Cumber, P.S., Fairweather. M., Falle, S.A.E.G. and Giddings, J.R., "Predictions of the Structure of Turbulent, Moderately Underexpanded Jets", Trans. ASME, Journal of Fluid Engineering, Vol.116, 1994, pp.703-713.

15. Birkby, P. and Page, G.J., "Numerical Predictions of Turbulent Underexpanded Sonic Jets Using a Pressure-based Methodology", Proceedings of IME - Part G - Journal of Aerospace Engineering, 2001, Vol.215 (3), pp.165-173

16. Wilkes, J.A., Glass, C.E., Danehy, P.M. and Nowak, R.J., "Fluorescence Imaging of Underexpanded Jets and Comparison with CFD", AIAA 2006-910.

17. GASP Version 4.0 User's Manual, Aerosoft, Inc., Blacksburg, VA, 2002, ISBN 09652780-5-0.

18. ANSYS CFX, Release 11.0: Installation and Overview, January, 2007.

19. Launder, B.E. and Spalding, D.B., "The Numerical Computation of Turbulent Flows", Computational Method in Applied Mechanical Engineering, Vol.3, 1974, pp.269-289.

20. Wilcox, D.C., "Multiscale Model for Turbulent Flows", AIAA Journal, Vol.26, No.11, pp.1311-1320.

21. Yakhot, V. and Orszag, S.A., "Renormalization Group Analysis of Turbulence", Journal of Scientific Computing, Vol.1, 1986, pp.3-51.

22. Menter, F.R., "Performance of Popular Turbulence Models for Attached and Separated Adverse Pressure Gradient Flows", AIAA Journal, Vol.30, No.8, 1992, pp.2066-2072.

23. Malsur Dharavath., Sinha, P.K. and Debasis Chakraborty., "Simulation of Supersonic Base Flow - Effect of Computational Grid and Turbulence Model", ASME Journal of Aerospace Engineering. Vol.224, No.3, 2010, pp.311-319.

24. Aswin, G. and Debasis Chakraborty., "Numerical Simulation of Transverse Side Jet Interaction with Supersonic Free Stream", Aerospace Sciences and Technologies Journal, Vol.14, 2010, pp. 295-301.

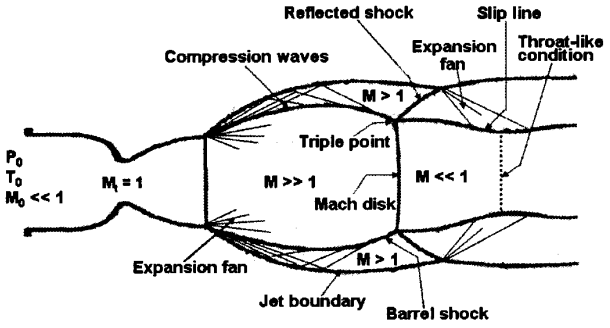

Fig.1 Schematic of Underexpanded Jet

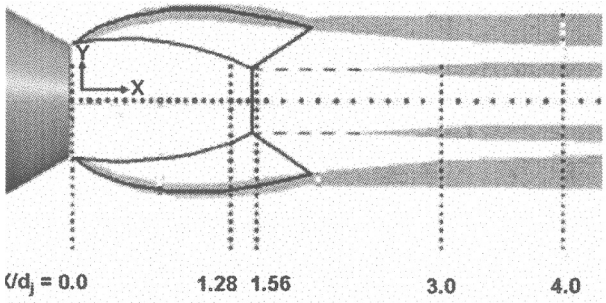

Fig.2 Axial Locations of Profile Measurements

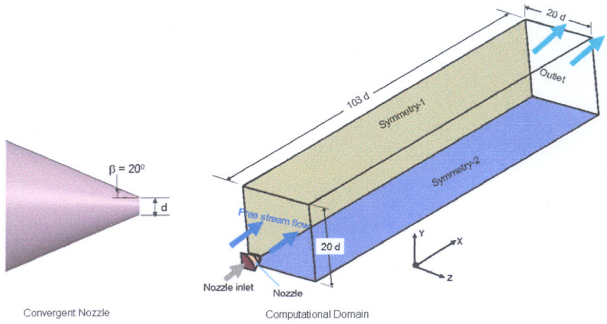

Fig.3 Nozzle Geometry and the Computational Domain

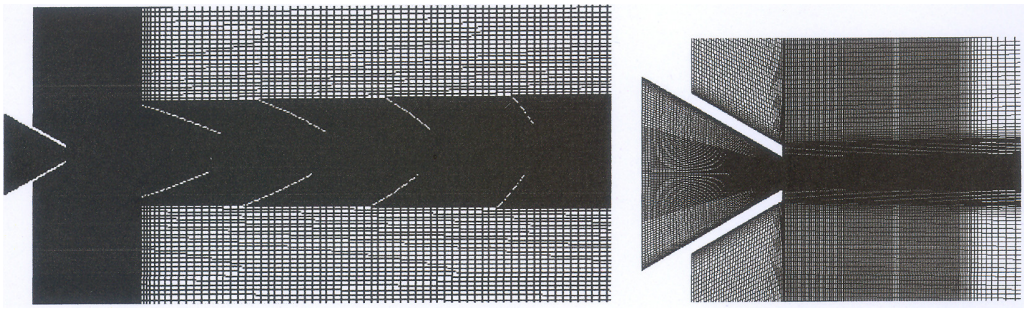

Fig.4 Grid Distribution on Symmetry Plane (Total Number of Nodes ~ 3.7 millions)

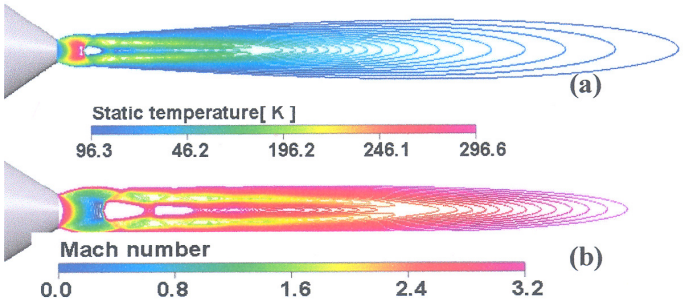

Fig.5 Flow Distribution in the Plane of Symmetry (a) Mach Number (b) Temperature

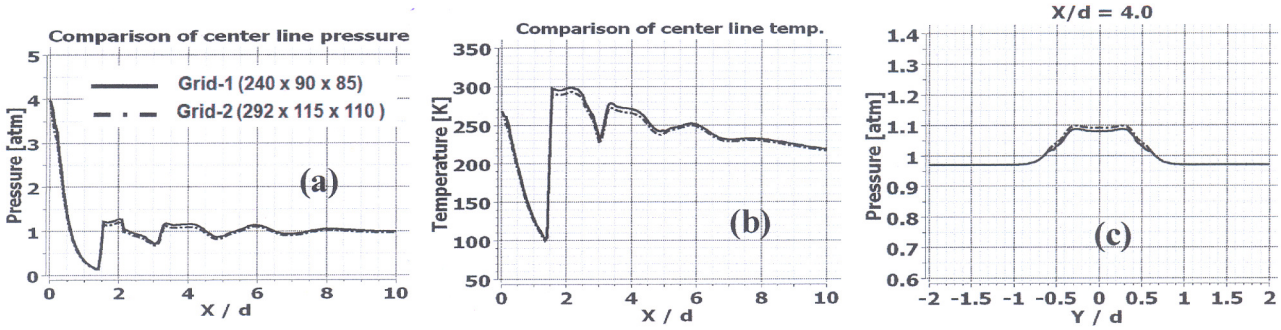

Fig.6 Comparison of (a) Pressure Distribution (b) Centerline Temperature Distribution and (c) Pressure Profile at x/D = 4.0 with Two Different Grids

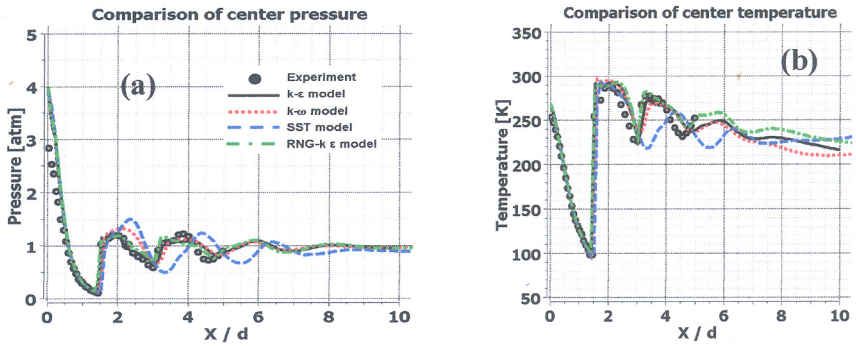

Fig.7 Comparison of Different Turbulence Models (a) Centerline Pressure (b) Centerline Temperature

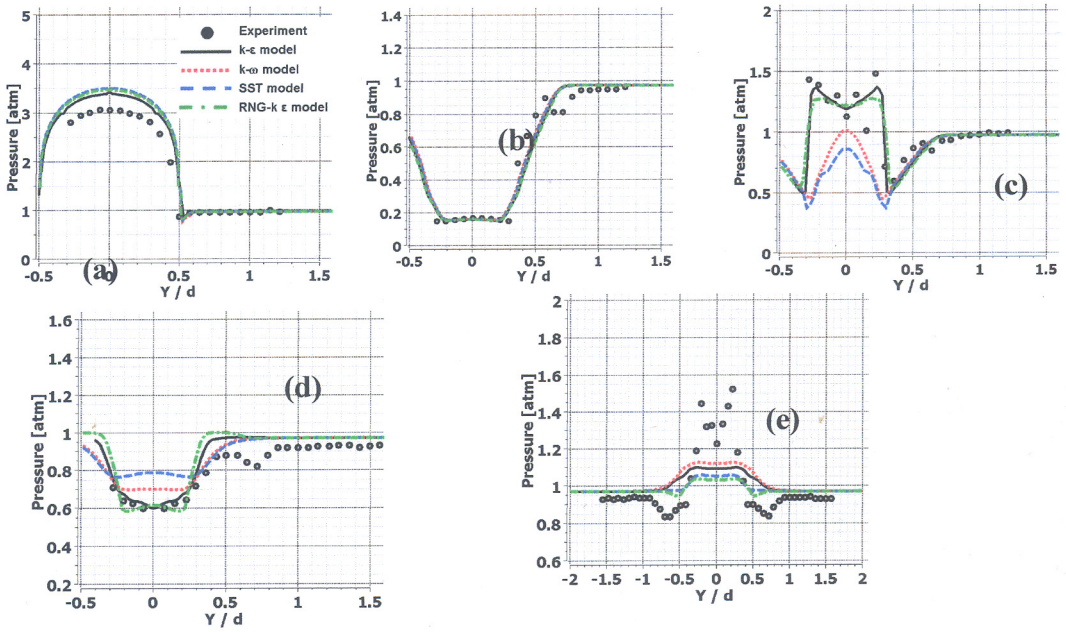

Fig.8 Comparison for Pressure Profiles with Different Turbulence Models
(a) x/d = 0 (b) x/d=1.28 (c) x/d=1.56 (d) x/d=3.0 and (e) x/d=4.0

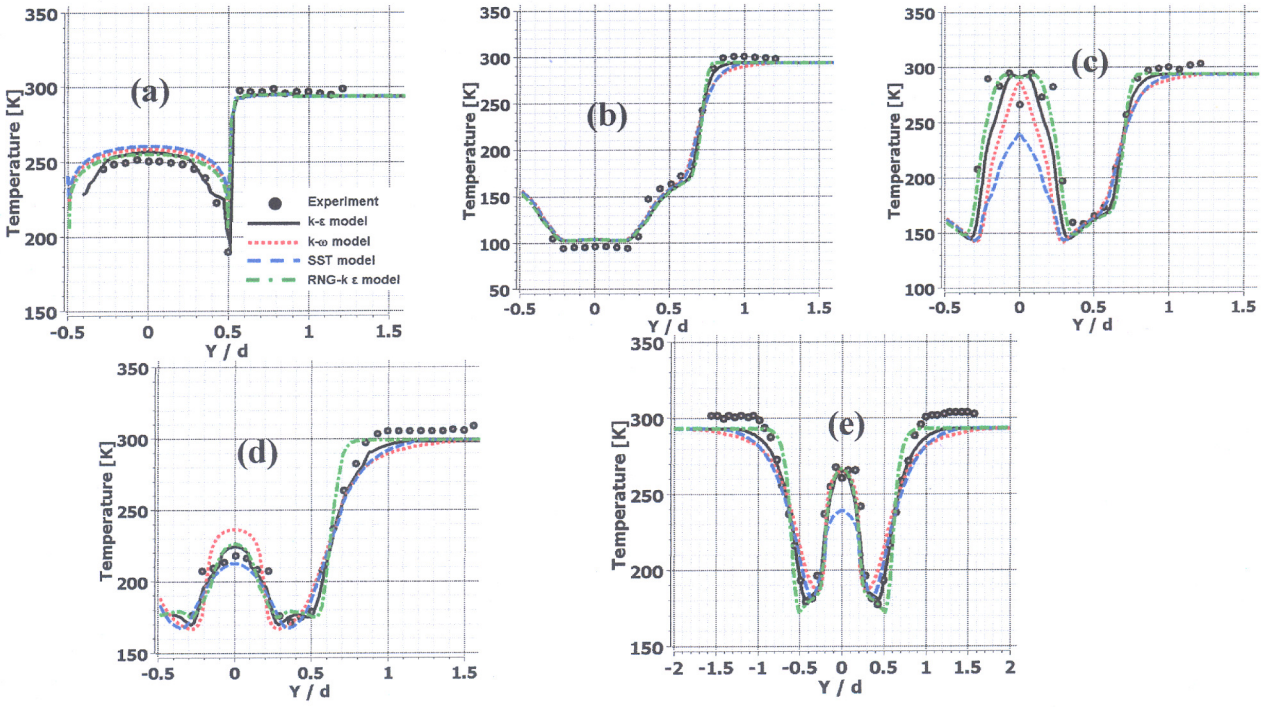

Fig.9 Comparison for Temperature Profiles with Different Turbulence Models
(a) x/d = 0 (b) x/d=1.28 (c) x/d=1.56 (d) x/d=3.0 and (e) x/d=4.0